symmetry

MDPI

Article

Quantum Hall and Shubnikov-de Haas Effects in Graphene within Non-Markovian Langevin Approach

Erkin Kh. Alpomishev [1,2], Gurgen G. Adamian [1,*] and Nikolay V. Antonenko [1,3]

[1] Bogoliubov Laboratory of Theoretical Physics, Joint Institute for Nuclear Research, 141980 Dubna, Russia; alpomishev@theor.jinr.ru (E.K.A.); antonenk@theor.jinr.ru (N.V.A.)
[2] Institute of Nuclear Physics, Tashkent 100214, Uzbekistan
[3] Tomsk Polytechnic University, 634050 Tomsk, Russia
* Correspondence: adamian@theor.jinr.ru

Abstract: The theory of open quantum systems is applied to study galvano-, thermo-magnetic, and magnetization phenomena in axial symmetric two-dimensional systems. Charge carriers are considered as quantum particles interacting with the environment through a one-body (mean-field) mechanism. The dynamics of charge carriers is affected by the average collision time that takes effectively into account two-body effects. The functional dependencies of the average collision time on the external uniform magnetic field, concentration and temperature are phenomenologically treated. Analytical expressions are obtained for the tensors of electric and thermal conductivity and/or resistivity. The developed theory is applied to describe the Shubnikov-de Haas oscillations and quantum Hall effect in graphene and GaAs/Al_xGa_{1-x}As heterostructure. The dependencies of magnetization and thermal conductivity on the magnetic field are also predicted.

Keywords: open quantum systems; electron mobility; non-Markovian dynamics; magnetic field; electric field; Shubnikov-de Haas oscillations; quantum Hall effect

Citation: Alpomishev, E.K.; Adamian, G.G.; Antonenko, N.V. Quantum Hall and Shubnikov-de Haas Effects in Graphene within Non-Markovian Langevin Approach. *Symmetry* **2024**, *16*, 7. https://doi.org/10.3390/sym16010007

Academic Editors: Charalampos Moustakidis and Jim Freericks

Received: 15 October 2023
Revised: 29 November 2023
Accepted: 13 December 2023
Published: 19 December 2023

1. Introduction

Emerging new two-dimensional (2D) materials such as heterostructures, graphene, and black phosphorus are considered promising candidates for next-generation electronic, optoelectronic devices, electrode materials, as well as for electrocatalysts in energy storage and electrocatalytic applications [1–5]. One of the fascinating topics in fundamental physics is experimental and theoretical investigations of the properties of 2D electron gas (2DEG) or 2D materials in uniform magnetic fields and at low temperatures. Since the charge carrier mobility in the 2D systems is significantly high, the quantum Hall effects (QHE) and the Shubnikov–de Haas oscillations (SdHO) were observed [6–13]. For example, the QHE appears in the bulk quasi-2D materials like the black-phosphorus [14,15] and the inorganic conductor molybdenum oxide [16] at temperatures of about 0.07–4 K. The oscillator behavior of the diagonal magneto-resistance and the quantization of the off-diagonal resistance R_{xy} at low temperature are interesting phenomena that have not yet been fully understood. External electric and magnetic fields and temperature can change the charge density, mobility, and collision time of charge carriers, as a result of which the transport properties of the latter may change [6]. At low temperatures and a sufficiently strong magnetic field, the SdHO amplitude is large and the QHE plateau is significantly wider [7,8]. For InSb single crystals with different concentrations and n-type mobility in the temperature range from $T_0 = 4.2$ to 16 K [8], the SdHO amplitude decreases with increasing temperature. It is also clear from the experiment that the period of oscillation remains unchanged at all temperatures. In ref. [13], the experiments with the $In_{0.53}Ga_{0.47}As/InP$ heterostructure were carried out at various low temperatures and found that the Hall plateau disappeared with increasing temperature. The half-width of the oscillations of the

diagonal resistance increases, which was also observed in graphene [17–26], which is a 2D material.

In ref. [17], the integer QHE was discovered in graphene at temperature $T_0 = 30$ mK. The experimental results obtained show that the mobility of charge carriers in graphene is very high. This, in turn, makes it possible to observe the QHE even at high temperatures. In ref. [20], they even managed to observe QHE under the influence of a very strong magnetic field at room temperature, where the Hall conductivity $\sigma_{xy} = 2e^2/h$ and the longitudinal conductivity $\sigma_{xx} = 0$. In ref. [17], the temperature dependence and gate-voltage (charge carriers concentration) dependence of the SdHO in graphene were measured. As obtained, the amplitude of SdHO significantly changes at the magnetic field $B \approx 5$ T. For the SdHO, it would be interesting to investigate theoretically the off-diagonal resistances R_{xy} that correspond to the experimentally obtained diagonal resistances R_{xx} at various magnetic fields and temperatures.

Experimental data show that graphene has a high thermal conductivity ($\kappa \simeq 3000$–5000 $\mathrm{Wm^{-1}K^{-1}}$ at room temperature) [24]. It depends on the type of substrate, defects, and concentration of impurity atoms [27–30]. Most experiments on thermal conductivity have usually been carried out at room temperature and higher. Therefore, we are interested in studying the dependence of thermal conductivity on the magnetic field at low temperatures using experimental data on electric conductivity.

In refs. [31–34], 2D systems in extremely strong magnetic fields were theoretically studied by treating the electron as a free particle and using a scattering potential with short- and long-range scatterers. This model does not work if the 2D system has too much surface roughness. In ref. [35], the Hall conductivity of 2D graphite was theoretically calculated using the Born approximation and analytical expressions for the Hall conductivities were obtained in the cases of short- and long-range scatterers and limits of strong and weak magnetic fields. To date, many experimental and theoretical studies have been carried out, but the theory of QHE is not fully developed.

The purpose of this work is to describe QHE and SdHO in graphene within the non-Markovian quantum Langevin formalism. The main idea of our model is as follows. The charge carriers are considered as quantum particles coupled to the environment (heat bath) through particle-phonon interactions. For example, the substrate of graphene can serve as a heat bath for it. The dynamics of the charge carriers are restricted by the average collision time. The functional forms of the average collision time and relaxation time on temperature, concentration, and magnetic field are extracted from experimental data. Because of this, in reality, the coupling used between the charge carrier and environment is actually more general than a simple particle-phonon coupling. In our model, the one-body, two-body, and non-Markovian effects are taken into consideration. Note, that the quantum Langevin approach was widely used to describe various macroscopic phenomena [36–46].

The work is organized as follows. In Section 2, the main assumptions of the model are discussed. The non-Markovian Langevin equations for the charge carriers embedded in the heat bath and uniform magnetic and electric fields are fully quantum-mechanically derived. Using the solutions of these equations, we obtain time-dependent expressions of the diagonal and non-diagonal electric conductivities in 2D systems. The resulting expressions were analyzed for weak and strong magnetic fields, as well as in the non-Markovian and Markovian limits. In Section 3, we present the description of experimental data on the QHE and SdHO in graphene and GaAs/$Al_xGa_{1-x}As$ heterostructure. The magnetization and thermal conductivity in graphene are predicted. In Section 4, the main conclusions are given.

2. Non-Markovian Langevin Equations in External Uniform Magnetic and Electric Fields

In order to derive the electric conductivity or resistance tensor for the 2D collective subsystem (charge carrier), a suitable microscopic Hamiltonian,

$$\begin{aligned} H &= H_c(B,E_x)+H_b+H_{cb}, \\ H_c &= \frac{1}{2m_x}(p_x-eA_x(x,y))^2+\frac{1}{2m_y}(p_y-eA_y(x,y))^2+eE_xx, \\ H_b &= \sum_\nu \hbar\omega_\nu b_\nu^+ b_\nu, \\ H_{cb} &= \sum_\nu(\alpha_\nu x+g_\nu y)(b_\nu^++b_\nu)+\sum_\nu\frac{1}{\hbar\omega_\nu}(\alpha_\nu x+g_\nu y)^2, \end{aligned} \tag{1}$$

was formulated in ref. [46]. The term H_c is the Hamiltonian of the collective subsystem embedded in the external uniform magnetic and electric fields. Here $\mathbf{q}=(x,y,0)$ is the collective coordinate of a charged particle and $\mathbf{p}=(p_x,p_y,0)$ is its canonically conjugated momentum, m_x and m_y are the components of the effective mass tensor, $\mathbf{A}=(-\frac{1}{2}yB,\frac{1}{2}xB,0)$ is the vector potential of the perpendicular axisymmetric magnetic field (along the z-axis) with the strength $B=|\mathbf{B}|$, and the constant electric field $\mathbf{E}=(E_x,0,0)$ acting in the x-axis direction (positive charge e). The terms H_b and H_{cb} are the Hamiltonians of the heat bath subsystem, and the collective-bath interaction with the coupling parameters α_ν and g_ν, respectively. The heat bath is an assembly of harmonic oscillators with frequencies ω_ν. The coupling to the heat bath is linear in the phonon creation b_ν^+ and annihilation b_ν operators and corresponds to the energy being transferred to and from the thermal reservoir by absorption or emission of bath quanta. We introduce the counter-term (second term) in H_{cb} in order to compensate for the coupling-induced potential [38,42].

Introducing new definitions for momenta

$$\pi_x=p_x+\frac{1}{2}m_x\omega_{cx}y,\ \ \pi_y=p_y-\frac{1}{2}m_y\omega_{cy}x, \tag{2}$$

where $\omega_{cx}=eB/m_x$ and $\omega_{cy}=eB/m_y$ ($\omega_c=\sqrt{\omega_{cx}\omega_{cy}}=\frac{eB}{\sqrt{m_xm_y}}$ is the cyclotron frequency), we rewrite the Hamiltonian H_c as

$$H_c = \frac{\pi_x^2}{2m_x}+\frac{\pi_y^2}{2m_y}+eE_xx. \tag{3}$$

Commuting the collective operators x, y, π_x, π_y, and the bath phonon operators b_ν, b_ν^+ with H, we obtain the system of the Heisenberg equations

$$\begin{aligned} \dot{x}(t) &= \frac{i}{\hbar}[H,x]=\frac{\pi_x(t)}{m_x}, \\ \dot{y}(t) &= \frac{i}{\hbar}[H,y]=\frac{\pi_y(t)}{m_y}, \\ \dot{\pi}_x(t) &= \frac{i}{\hbar}[H,\pi_x] \\ &= \pi_y(t)\omega_{cy}-eE_x-\sum_\nu\alpha_\nu(b_\nu^+(t)+b_\nu(t))-2\sum_\nu\frac{\alpha_\nu}{\hbar\omega_\nu}[\alpha_\nu x(t)+g_\nu y(t)], \\ \dot{\pi}_y(t) &= \frac{i}{\hbar}[H,\pi_y] \\ &= -\pi_x(t)\omega_{cx}-\sum_\nu g_\nu(b_\nu^+(t)+b_\nu(t))-2\sum_\nu\frac{g_\nu}{\hbar\omega_\nu}[\alpha_\nu x(t)+g_\nu y(t)], \end{aligned} \tag{4}$$

and

$$\begin{aligned}\dot{b}_\nu^+(t) &= \frac{i}{\hbar}[H, b_\nu^+] = i\omega_\nu b_\nu^+(t) + \frac{i}{\hbar}(\alpha_\nu x(t) + g_\nu y(t)),\\ \dot{b}_\nu(t) &= \frac{i}{\hbar}[H, b_\nu] = -i\omega_\nu b_\nu(t) - \frac{i}{\hbar}(\alpha_\nu x(t) + g_\nu y(t)).\end{aligned} \tag{5}$$

Substituting the solution

$$\begin{aligned}b_\nu^+(t) &= f_\nu^+(t) - \frac{\alpha_\nu x(t) + g_\nu y(t)}{\hbar\omega_\nu}\\ &+ \frac{\alpha_\nu}{\hbar\omega_\nu}\int_0^t d\tau \dot{x}(\tau) e^{i\omega_\nu(t-\tau)} + \frac{g_\nu}{\hbar\omega_\nu}\int_0^t d\tau \dot{y}(\tau) e^{i\omega_\nu(t-\tau)},\\ b_\nu(t) &= f_\nu(t) - \frac{\alpha_\nu x(t) + g_\nu y(t)}{\hbar\omega_\nu}\\ &+ \frac{\alpha_\nu}{\hbar\omega_\nu}\int_0^t d\tau \dot{x}(\tau) e^{-i\omega_\nu(t-\tau)} + \frac{g_\nu}{\hbar\omega_\nu}\int_0^t d\tau \dot{y}(\tau) e^{-i\omega_\nu(t-\tau)},\\ f_\nu(t) &= [b_\nu(0) + \frac{\alpha_\nu x(0) + g_\nu y(0)}{\hbar\omega_\nu}]e^{-i\omega_\nu t}\end{aligned} \tag{6}$$

of Equation (5) into (4), we obtain the stochastic dissipative quantum Langevin equations (Heisenberg–Langevin equations)

$$\begin{aligned}\dot{x}(t) &= \frac{\pi_x(t)}{m_x},\\ \dot{y}(t) &= \frac{\pi_y(t)}{m_y},\\ \dot{\pi}_x(t) &= \pi_y(t)\omega_{cy} - eE_x - \frac{1}{m_x}\int_0^t d\tau K_\alpha(t-\tau)\pi_x(\tau) - \frac{1}{m_y}\int_0^t d\tau K_{\alpha g}(t-\tau)\pi_y(\tau) + F_\alpha(t),\\ \dot{\pi}_y(t) &= -\pi_x(t)\omega_{cx} - \frac{1}{m_y}\int_0^t d\tau K_g(t-\tau)\pi_y(\tau) - \frac{1}{m_x}\int_0^t d\tau K_{g\alpha}(t-\tau)\pi_y(\tau) + F_g(t)\end{aligned} \tag{7}$$

with the dissipative kernels

$$\begin{aligned}K_\alpha(t-\tau) &= \sum_\nu \frac{2\alpha_\nu^2}{\hbar\omega_\nu}\cos[\omega_\nu(t-\tau)],\ \ K_g(t-\tau) = \sum_\nu \frac{2g_\nu^2}{\hbar\omega_\nu}\cos[\omega_\nu(t-\tau)],\\ K_{\alpha g}(t-\tau) &= K_{g\alpha}(t-\tau) = \sum_\nu \frac{2\alpha_\nu g_\nu}{\hbar\omega_\nu}\cos[\omega_\nu(t-\tau)],\end{aligned} \tag{8}$$

and the random forces

$$\begin{aligned}F_\alpha(t) &= -\sum_\nu F_\alpha^\nu(t) = -\sum_\nu \alpha_\nu(f_\nu^+(t) + f_\nu(t)),\\ F_g(t) &= -\sum_\nu F_g^\nu(t) = -\sum_\nu g_\nu(f_\nu^+(t) + f_\nu(t))\end{aligned} \tag{9}$$

in the coordinates. The random force operators $F_\alpha^\nu(t)$ and $F_g^\nu(t)$ are identified as fluctuations are identified as fluctuations due to the uncertainty of the initial conditions for the thermostat operators. We consider an ensemble of initial states in which the operators of the collective subsystem are fixed at the values $x(0)$ and $y(0)$, and the initial bath operators are drawn from an ensemble that is canonical relative to the collective subsystem [39,42]. The initial distribution is then the conditional density matrix $\rho_0(\{b_\nu^+(0), b_\nu(0)\}|\mathbf{q}(0)) = \exp(-\sum_\nu \hbar\omega_\nu[b_\nu^+ + \frac{\alpha_\nu x + g_\nu y}{\hbar\omega_\nu}][b_\nu + \frac{\alpha_\nu x + g_\nu y}{\hbar\omega_\nu}]/T_0)/Z(T_0)$, where

$Z(T_0)$ is conditional partition function. In an ensemble of initial states for the bath operators, the fluctuations $F_\alpha^\nu(t)$ and $F_g^\nu(t)$ have the Gaussian distributions with zero average value

$$\ll F_\alpha^\nu(t) \gg = \ll F_g^\nu(t) \gg = 0, \tag{10}$$

where the symbol $\ll \ldots \gg$ denotes the average over the bath. The temperature T_0 of the heat bath is included in the analysis through the distribution of initial conditions. The Bose-Einstein statistics is employed for the heat bath:

$$\begin{aligned} \ll f_\nu^+(t) f_{\nu'}^+(t') \gg &= \ll f_\nu(t) f_{\nu'}(t') \gg = 0, \\ \ll f_\nu^+(t) f_{\nu'}(t') \gg &= \delta_{\nu,\nu'} n_\nu e^{i\omega_\nu (t-t')}, \\ \ll f_\nu(t) f_{\nu'}^+(t') \gg &= \delta_{\nu,\nu'} (n_\nu + 1) e^{-i\omega_\nu (t-t')}, \end{aligned} \tag{11}$$

where $n_\nu = [\exp(\hbar\omega_\nu / T_0) - 1]^{-1}$ are the occupation numbers for phonons. Employing (11), the quantum fluctuation-dissipation relations are obtained:

$$\sum_\nu \varphi_{\alpha\alpha}^\nu(t,t') \frac{\tanh[\frac{\hbar\omega_\nu}{2T_0}]}{\hbar\omega_\nu} = K_\alpha(t-t'), \ \sum_\nu \varphi_{gg}^\nu(t,t') \frac{\tanh[\frac{\hbar\omega_\nu}{2T_0}]}{\hbar\omega_\nu} = K_g(t-t'),$$

$$\sum_\nu \varphi_{\alpha g}^\nu(t,t') \frac{\tanh[\frac{\hbar\omega_\nu}{2T_0}]}{\hbar\omega_\nu} = K_{\alpha g}(t-t'),$$

where

$$\varphi_{\alpha\alpha}^\nu(t,t') = 2\alpha_\nu^2 [2n_\nu + 1] \cos(\omega_\nu [t-t']), \ \ \varphi_{gg}^\nu(t,t') = 2g_\nu^2 [2n_\nu + 1] \cos(\omega_\nu [t-t']),$$

$$\varphi_{\alpha g}^\nu(t,t') = 2\alpha_\nu g_\nu [2n_\nu + 1] \cos(\omega_\nu [t-t']),$$

are the symmetrized correlation functions $\varphi_{kk'}^\nu(t,t') = \ll F_k^\nu(t) F_{k'}^\nu(t') + F_{k'}^\nu(t') F_k^\nu(t) \gg$, $k, k' = \alpha, g$. The quantum fluctuation-dissipation relations are reduced to the classical ones in the high-temperature limit (or $\hbar \to 0$): $\sum_\nu \varphi_{\alpha\alpha}^\nu(t,t') = 2T_0 K_\alpha(t-t')$, $\sum_\nu \varphi_{gg}^\nu(t,t') = 2T_0 K_g(t-t')$, and $\sum_\nu \varphi_{\alpha g}^\nu(t,t') = 2T_0 K_{\alpha g}(t-t')$.

The presence of the integral parts in Equation (7) indicates non-Markovian dynamics of the system. The dissipative kernels have the form of memory functions since they make the equations of motion at time t dependent on the values of $\dot{x}$ and $\dot{y}$ for previous times. The Laplace transform $\hat{L}$ of Equation (7) leads to the system of linear equations:

$$\begin{aligned} x(s)s &= x(0) + \frac{\pi_x(s)}{m_x}, \\ y(s)s &= y(0) + \frac{\pi_y(s)}{m_y}, \\ \pi_x(s)s &= \pi_x(0) + \omega_{cy}\pi_y(s) - \frac{eE_x}{s} - K_\alpha(s)\frac{\pi_x(s)}{m_x} - K_{\alpha g}(s)\frac{\pi_y(s)}{m_y} + F_\alpha(s), \\ \pi_y(s)s &= \pi_y(0) - \omega_{cx}\pi_x(s) - K_g(s)\frac{\pi_y(s)}{m_y} - K_{g\alpha}(s)\frac{\pi_x(s)}{m_x} + F_g(s). \end{aligned} \tag{12}$$

Here, $K_\alpha(s)$, $K_g(s)$, $K_{\alpha g}(s)$, $K_{g\alpha}(s)$ and $F_\alpha(s)$, $F_g(s)$ are the Laplace transforms of the dissipative kernels and random forces, respectively. The system of Equation (12) is easy to solve and performs the inverse Laplace transform $\hat{L}^{-1}$ using the residue theorem and the roots of the determinant

$$\begin{aligned} D &= s^2 + \omega_{cx}\omega_{cy} + \frac{sK_\alpha(s)}{m_x} + \frac{sK_g(s)}{m_y} + \frac{\omega_{cy}K_{g\alpha}(s)}{m_x} \\ &- \frac{\omega_{cx}K_{\alpha g}(s)}{m_y} + \frac{K_\alpha(s)K_g(s)}{m_x m_y} - \frac{K_{\alpha g}(s)K_{g\alpha}(s)}{m_x m_y} = 0. \end{aligned} \tag{13}$$

Finally, the explicit solutions for the originals are

$$\begin{aligned} x(t) &= x(0) + A_1(t)\pi_x(0) + A_2(t)\pi_y(0) - A_3(t)eE_x + I_x(t) + I'_x(t), \\ y(t) &= y(0) + B_1(t)\pi_y(0) - B_2(t)\pi_x(0) + B_3(t)eE_x - I_y(t) + I'_y(t), \\ \pi_x(t) &= C_1(t)\pi_x(0) + C_2(t)\pi_y(0) - C_3(t)eE_x + I_{\pi_x}(t) + I'_{\pi_x}(t), \\ \pi_y(t) &= D_1(t)\pi_y(0) - D_2(t)\pi_x(0) + D_3(t)eE_x - I_{\pi_y}(t) + I'_{\pi_y}(t). \end{aligned} \tag{14}$$

In Equation (14),

$$I_x(t) = \int_0^t A_1(\tau)F_\alpha(t-\tau)d\tau, I'_x(t) = \int_0^t A_2(\tau)F_g(t-\tau)d\tau, I_y(t) = \int_0^t B_2(\tau)F_\alpha(t-\tau)d\tau,$$

$$I'_y(t) = \int_0^t B_1(\tau)F_g(t-\tau)d\tau, I_{\pi_x}(t) = \int_0^t C_1(\tau)F_\alpha(t-\tau)d\tau, I'_{\pi_x}(t) = \int_0^t C_2(\tau)F_g(t-\tau)d\tau,$$

$$I_{\pi_y}(t) = \int_0^t D_2(\tau)F_\alpha(t-\tau)d\tau, I'_{\pi_y}(t) = \int_0^t D_1(\tau)F_g(t-\tau)d\tau,$$

and the time-dependent coefficients

$$\begin{aligned} A_1(t) &= \hat{L}^{-1}\left[\frac{m_y s + K_g(s)}{m_x m_y D(s)s}\right] = B_1|_{x,\alpha\leftrightarrow y,g}, \; A_2(t) = \hat{L}^{-1}\left[\frac{m_y\omega_{cy} - K_{\alpha g}(s)}{m_x m_y D(s)s}\right], \\ A_3(t) &= \hat{L}^{-1}\left[\frac{m_y s + K_g(s)}{m_x m_y D(s)s^2}\right], \; B_2(t) = \hat{L}^{-1}\left[\frac{m_x\omega_{cx} + K_{g\alpha}(s)}{m_x m_y D(s)s}\right], \\ B_3(t) &= \hat{L}^{-1}\left[\frac{m_x\omega_{cx} + K_{g\alpha}(s)}{m_x m_y D(s)s^2}\right], \; C_1(t) = \hat{L}^{-1}\left[\frac{m_y s + K_g(s)}{m_y D(s)}\right] = D_1|_{x,\alpha\leftrightarrow y,g}, \\ C_2(t) &= \hat{L}^{-1}\left[\frac{m_y\omega_{cy} - K_{\alpha g}(s)}{m_y D(s)}\right], \; C_3(t) = \hat{L}^{-1}\left[\frac{m_y s + K_g(s)}{m_y D(s)s}\right], \\ D_2(t) &= \hat{L}^{-1}\left[\frac{m_x\omega_{cx} + K_{g\alpha}(s)}{m_x D(s)}\right], \; D_3(t) = \hat{L}^{-1}\left[\frac{m_x\omega_{cx} + K_{g\alpha}(s)}{m_x D(s)s}\right]. \end{aligned} \tag{15}$$

In general, the diagonal dissipative kernels are much larger than off-diagonal ones. For simplicity, we assume that there is no correlation between the operators F^ν_α and F^ν_g, so that $K_{\alpha g} = K_{g\alpha} = 0$. We introduce the spectral density D_ω of the heat bath excitations to replace the sum over ν by the integral over frequency ω: $\sum_\nu \ldots \to \int_0^\infty d\omega D_\omega \ldots$, $\alpha_\nu \to \alpha_\omega$, $g_\nu \to g_\omega$, $\omega_\nu \to \omega$, and $n_\nu \to n_\omega$. The well-known spectral functions [36,39,42]

$$D_\omega\frac{\alpha^2_\omega}{\omega} = \frac{\lambda^2_x}{\pi}\frac{\gamma^2}{\gamma^2+\omega^2}, \; D_\omega\frac{g^2_\omega}{\omega} = \frac{\lambda^2_y}{\pi}\frac{\gamma^2}{\gamma^2+\omega^2} \tag{16}$$

are used. Here, the memory time γ^{-1} of dissipation is inverse to the phonon bandwidth of the heat bath excitations and the coefficients

$$\lambda_x = \frac{1}{m_x}\int_0^\infty d\tau K_\alpha(t-\tau), \; \lambda_y = \frac{1}{m_y}\int_0^\infty d\tau K_g(t-\tau)$$

are the friction coefficients in the Markovian limit. This Ohmic dissipation with the Lorenzian cutoff (Drude dissipation) results in the dissipative kernels

$$K_\alpha(t) = m_x\lambda_x\gamma e^{-\gamma|t|}, \quad K_g(t) = m_y\lambda_y\gamma e^{-\gamma|t|}. \tag{17}$$

So, the solutions for the collective coordinates (14) include the following time-dependent coefficients

$$\begin{aligned}
A_1(t) &= \dot{A}_3(t), \quad A_2(t) = \dot{B}_3(t)|_{x\leftrightarrow y},\\
A_3(t) &= \frac{1}{m_x}\left(\frac{\lambda_y t}{\omega_c^2+\lambda_x\lambda_y} + \frac{\omega_c^2(\gamma-\lambda_y)-\lambda_y^2(\gamma-\lambda_x)}{\gamma\left(\omega_c^2+\lambda_x\lambda_y\right)^2}\right.\\
&+ \left.\sum_{i=1}^{4}\frac{\beta_i(s_i+\gamma)\left(\gamma\lambda_y+s_i(s_i+\gamma)\right)e^{s_i t}}{s_i^2}\right),\\
B_1(t) &= \dot{A}_3(t)|_{x\leftrightarrow y}, \quad B_2(t) = \dot{B}_3(t),\\
B_3(t) &= \frac{\omega_{cx}}{m_y}\left(\frac{t}{\omega_c^2+\lambda_x\lambda_y} + \frac{2\lambda_x\lambda_y-\gamma(\lambda_x+\lambda_y)}{\gamma\left(\omega_c^2+\lambda_x\lambda_y\right)^2} + \sum_{i=1}^{4}\frac{\beta_i(s_i+\gamma)^2 e^{s_i t}}{s_i^2}\right),\\
C_1(t) &= m_x\ddot{A}_3(t), \quad C_2(t) = m_x\ddot{B}_3(t)|_{x\leftrightarrow y}, \quad C_3(t) = m_x\dot{A}_3(t),\\
D_1(t) &= C_1(t)|_{x\leftrightarrow y}, \quad D_2(t) = C_2(t)|_{x\leftrightarrow y}, \quad D_3(t) = m_y\dot{B}_3(t),
\end{aligned} \tag{18}$$

where $\beta_i = [\prod_{j\neq i}(s_i - s_j)]^{-1}$ $(i,j = 1-4)$ and s_i are the roots of the equation

$$D(s) = (s+\gamma)\Big[(s^2+\omega_c^2)(s+\gamma) + s\gamma\lambda_x\Big] + \gamma\lambda_y[s(s+\gamma)+\gamma\lambda_x] = 0. \tag{19}$$

These roots arise when the residue theorem is applied to perform the integration in the inverse Laplace transform $\hat{L}^{-1}$.

The system of equations for the first moments

$$\begin{aligned}
\langle\dot{x}(t)\rangle &= \frac{\langle\pi_x(t)\rangle}{m_x}, \quad \langle\dot{y}(t)\rangle = \frac{\langle\pi_y(t)\rangle}{m_y}\\
\langle\dot{\pi}_x(t)\rangle &= \tilde{\omega}_{cy}(t)\langle\pi_y(t)\rangle - \lambda_{\pi_x}(t)\langle\pi_x(t)\rangle - e\tilde{E}_{xx}(t),\\
\langle\dot{\pi}_y(t)\rangle &= -\tilde{\omega}_{cx}(t)\langle\pi_x(t)\rangle - \lambda_{\pi_y}(t)\langle\pi_y(t)\rangle - e\tilde{E}_{xy}(t)
\end{aligned} \tag{20}$$

is derived by averaging Equation (14) over the entire system and differentiating them with respect to t. In Equation (20),

$$\begin{aligned}
\lambda_{\pi_x}(t) &= -\frac{D_1(t)\dot{C}_1(t)+D_2(t)\dot{C}_2(t)}{C_1(t)D_1(t)+C_2(t)D_2(t)},\\
\lambda_{\pi_y}(t) &= -\frac{C_1(t)\dot{D}_1(t)+C_2(t)\dot{D}_2(t)}{C_1(t)D_1(t)+C_2(t)D_2(t)},
\end{aligned} \tag{21}$$

$$\begin{aligned}
\tilde{\omega}_{cx}(t) &= \frac{D_1(t)\dot{D}_2(t)-D_2(t)\dot{D}_1(t)}{C_1(t)D_1(t)+C_2(t)D_2(t)},\\
\tilde{\omega}_{cy}(t) &= \frac{C_1(t)\dot{C}_2(t)-C_2(t)\dot{C}_1(t)}{C_1(t)D_1(t)+C_2(t)D_2(t)},
\end{aligned} \tag{22}$$

and

$$\begin{aligned}
\tilde{E}_{xx}(t) &= E_x\left[D_3(t)\tilde{\omega}_{cy} + C_3(t)\lambda_{\pi_x}(t) + \dot{C}_3(t)\right],\\
\tilde{E}_{xy}(t) &= E_x\Big[C_3(t)\tilde{\omega}_{cx} - D_3(t)\lambda_{\pi_y}(t) - \dot{D}_3(t)\Big]
\end{aligned} \tag{23}$$

are the friction coefficients, renormalized cyclotron frequencies, and the components of the electric field, respectively. As seen, the cross-component (along the y-axis) of the electric field $\tilde{E}_{xy}(t)$ is equal to zero at $t = 0$ and only arises during the non-Markovian evolution of charge carriers, and $\tilde{E}_{xy}(t \to \infty) \neq 0$ (the classical Hall effect). Note that $\tilde{E}_{xy}(t) = 0$ in the Markovian limit ($\gamma \to \infty$) [46].

One can define the current density ($k, l = x, y$) [6]

$$J_k = \sum_l \sigma_{kl}(B) E_l \tag{24}$$

by using the expression $\mathbf{J} = ne\langle \dot{\mathbf{q}}(t) \rangle$ and Equation (20):

$$J_x = \frac{ne^2}{m_x} C_3(t) E_x(t), \quad J_y = -\frac{ne^2}{m_y} D_3(t) E_x(t). \tag{25}$$

Changing the direction of the electric field $\mathbf{E} = (E_x, 0, 0)$ to $\mathbf{E} = (0, E_y, 0)$, we obtain

$$J_x = \frac{ne^2}{m_x} \tilde{D}_3(t) E_y(t), \quad J_y = \frac{ne^2}{m_y} \tilde{C}_3(t) E_y(t), \tag{26}$$

where

$$\tilde{C}_3(t) = m_y L^{-1}\left[\frac{K_{xx}(s) + m_x s}{D}\right], \quad \tilde{D}_3 = m_x m_y \omega_{cy} L^{-1}\left[\frac{1}{D}\right]. \tag{27}$$

From (24)–(26) we obtain the expression for the conductivity tensor

$$\sigma(\tau) = ne^2 \begin{pmatrix} \frac{C_3(\tau)}{m_x} & -\frac{D_3(\tau)}{m_y} \\ \frac{\tilde{D}_3(\tau)}{m_x} & \frac{\tilde{C}_3(\tau)}{m_y} \end{pmatrix} \tag{28}$$

at time τ. The inverse transformation of $\sigma(\tau)$ results in the resistance tensor

$$R(\tau) = \frac{1}{ne^2\left[C_3(\tau)\tilde{C}_3(\tau) + D_3(\tau)\tilde{D}_3(\tau)\right]} \begin{pmatrix} m_x \tilde{C}_3(\tau) & m_x D_3(\tau) \\ -m_y \tilde{D}_3(\tau) & m_y C_3(\tau) \end{pmatrix}. \tag{29}$$

The non-diagonal elements

$$R_H(\tau) = \frac{m_x D_3(\tau)}{ne^2\left[C_3(\tau)\tilde{C}_3(\tau) + D_3(\tau)\tilde{D}_3(\tau)\right]} = \frac{m_y \tilde{D}_3(\tau)}{ne^2\left[C_3(\tau)\tilde{C}_3(\tau) + D_3(\tau)\tilde{D}_3(\tau)\right]} \tag{30}$$

of the $R(\tau)$ have the meaning of the Hall resistance.

In order to describe the magnetotransport in real 2D systems, we need to use some additional assumptions [46]:

(1) The dynamics of charge carriers are determined by three main characteristic times: the relaxation time $\tau_r = \lambda^{-1}$ (if $\lambda_x = \lambda_y = \lambda$), the average time τ of a free path (or the average collision time of a charge carrier between two successive collisions with ions/atoms of the lattice), and the memory time γ^{-1} of the heat bath excitations. The values of τ_r and τ are associated with one-body (mean-field) and two-body dissipations (effects), respectively (see Figure 1). At $\tau \gg \tau_r$ ($\tau_r \gg \tau$), one-body (two-body) dissipation dominates. If the values of τ_r and τ are comparable, then the transition process takes place. In general, the values of τ_r and τ depend on the magnetic field B, temperature T_0, and concentration n. Since these relationships are extracted from known experimental data, the coupling used between the charge carrier and environment is actually more general than the particle-phonon interaction.

(2) Since the mass of the charge carrier is negligibly small compared to the mass of the ion/atom, it can be assumed that with each collision with the ion/atom, the charge carrier completely loses its ordered motion and its velocity or momentum becomes equal to zero. The times τ of a free path are assumed to be the same for all charge carriers and all collisions. Thus, the time limit $t = \tau$ is introduced in the conductivity tensor (28) or resistance tensor (29).

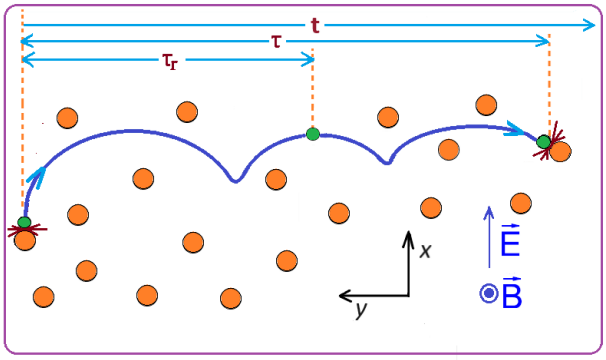

Figure 1. Schematic illustration of the motion (time arrow t indicated) of the charge carrier (small green circle) between two successive collisions with ions/atoms (large brown circles) of the lattice as well as the relaxation time τ_r and the average collision time τ scales in 2D magnetotransport. Uniform magnetic field $\mathbf{B} = (0, 0, B)$ perpendicular to the xy plane (along the z-axis), and the constant electric field $\mathbf{E} = (E_x, 0, 0)$ acts in the direction of the x-axis.

For the space-symmetric system ($m_x = m_y = m$, $\lambda_x = \lambda_y = \lambda$), we derive analytical expressions that help us clarify our model and the magnetotransport process. In this case, Equation (19) simplifies as

$$\left(s^2 + \omega_c^2\right)(\gamma + s)^2 + 2\gamma\lambda s(\gamma + s) + \lambda^2\gamma^2 = 0. \tag{31}$$

The roots of this equation are

$$\begin{aligned} s_1 &= -\frac{1}{2}\left(\gamma + i\omega_c + \sqrt{(\gamma - i\omega_c)^2 - 4\gamma\lambda}\right), \; s_2 = s_1^*, \\ s_3 &= -\frac{1}{2}\left(\gamma + i\omega_c - \sqrt{(\gamma - i\omega_c)^2 - 4\gamma\lambda}\right), \; s_4 = s_3^*. \end{aligned}$$

Expanding these roots up to the first order in λ/γ,

$$s_1 = s_2^* = -\gamma\frac{\omega_c^2 + \gamma^2 - \gamma\lambda}{\gamma^2 + \omega_c^2} + i\frac{\lambda\gamma\omega_c}{\gamma^2 + \omega_c^2}, \; s_3 = s_4^* = -\frac{\lambda\gamma^2}{\gamma^2 + \omega_c^2} - i\frac{\omega_c^2 + \gamma^2 + \gamma\lambda}{\gamma^2 + \omega_c^2}\omega_c, \tag{32}$$

and taking them at $t = \tau$, we obtain the diagonal and off-diagonal components of conductivity

$$\begin{aligned} \sigma_{xx}(\tau) &= \frac{\sigma_{xx0}}{1 + (\omega_c\tau_r)^2} - \frac{\sigma_{xx0}}{\sqrt{1 + (\omega_c\tau_r)^2}} \\ &\times \exp[-\frac{\gamma^2}{\gamma^2 + \omega_c^2}\frac{\tau}{\tau_r}]\cos[\frac{(\gamma^2 + \gamma/\tau_r + \omega_c^2)\omega_c\tau}{\gamma^2 + \omega_c^2} + \arctan(\omega_c\tau_r)], \\ \sigma_{xy}(\tau) &= -\frac{\sigma_{xx0}\omega_c\tau_r}{1 + (\omega_c\tau_r)^2} + \frac{\sigma_{xx0}}{\sqrt{1 + (\omega_c\tau_r)^2}} \\ &\times \exp[-\frac{\gamma^2}{\gamma^2 + \omega_c^2}\frac{\tau}{\tau_r}]\cos[\frac{(\gamma^2 + \gamma/\tau_r + \omega_c^2)\omega_c\tau}{\gamma^2 + \omega_c^2} - \arctan(\frac{1}{\omega_c\tau_r})]. \end{aligned} \tag{33}$$

As seen, Equation (33) contain the non-oscillatory and oscillatory components. If the values of τ_r and τ are comparable, the non-oscillatory terms of (33) have a major role. In the Markovian limit ($\gamma \to \infty$), Equation (33) are transformed to simpler expressions:

$$\begin{aligned}\sigma_{xx}(\tau) &= \frac{\sigma_{xx0}}{1+(\omega_c\tau_r)^2} - \frac{\sigma_{xx0}}{\sqrt{1+(\omega_c\tau_r)^2}}\exp[-\frac{\tau}{\tau_r}]\cos[\omega_c\tau + \arctan(\omega_c\tau_r)],\\ \sigma_{xy}(\tau) &= -\frac{\sigma_{xx0}\omega_c\tau_r}{1+(\omega_c\tau_r)^2} + \frac{\sigma_{xx0}}{\sqrt{1+(\omega_c\tau_r)^2}}\exp[-\frac{\tau}{\tau_r}]\cos[\omega_c\tau - \arctan(\frac{1}{\omega_c\tau_r})].\end{aligned} \quad (34)$$

At $\tau \gg \tau_r$ or $t \to \infty$, the oscillatory terms vanish and we obtain the Drude conductivity tensor

$$\sigma = \frac{\sigma_{xx0}}{1+(\omega_c\tau_r)^2}\begin{pmatrix} 1 & -\omega_c\tau_r \\ \omega_c\tau_r & 1 \end{pmatrix} \quad (35)$$

with the Drude conductivity

$$\sigma_{xx0} = \frac{ne^2\tau_r}{m} \quad (36)$$

at $B = 0$. Thus, one can say that our model is the generalized Drude model.

3. Calculated Results

In order to turn to the observable values, all parameters τ^{-1}, τ_r^{-1}, ω_c, and γ in the expressions are multiplied by m/e:

$$\begin{aligned}\tau^{-1} \to \frac{m}{e}\tau^{-1}, \quad \tau_r^{-1} \to \frac{m}{e}\tau_r^{-1} = \mu^{-1},\\ \omega_c \to \frac{m}{e}\omega_c = B, \quad \gamma \to \frac{m}{e}\gamma = \Gamma.\end{aligned} \quad (37)$$

So instead of the friction coefficient λ, cyclotron frequency ω_c, and the inverse response time γ of the system, we have the inverse reciprocal mobility μ^{-1} of charge carriers, the strength of the magnetic field B, and a new parameter Γ related to the memory time. However, for the graphene and 2D heterostructures considered, the mobility is almost independent of B (here $\mu(B) = \mu_0$ and $\mu_0 = \mu(B = 0)$) in a wide range of B. So, their properties are described by neglecting the effect of the magnetic field on the coupling term.

3.1. SdHO and QHE

The dependence of magnetoresistance (R_{xx}) and Hall resistance (R_{xy}) on the magnetic field is shown in Figure 2 for a wide range of magnetic fields. Experimental results are taken from ref. [17], and theoretical calculations are performed using formula (29) with $\Gamma = 13/(\tau/\tau_r)$. The experiment is conducted at the temperature $T_0 = 30$ mK and the gate voltage $V_g = 15$ V applied to the graphene sample. The charge carriers consist of electrons and they have very high mobility, which is μ = 13,000 $\mathrm{cm^2V^{-1}s^{-1}}$ and it weakly depends on the magnetic field and temperature. The SiO_2 is taken as a substrate, and the carrier density is controlled by applying a gate voltage V_g ($n = \alpha V_g$, where $\alpha \approx 7.3 \times 10^{10}$ $\mathrm{cm^{-2}V^{-1}}$ [19]). The average collision times τ are extracted using the experimental data.

In Figure 2, the SdHO is observed in a narrow range of magnetic fields ($B \leq 3$ T), and the QHE is observed at strong magnetic fields ($B > 3$ T), where the longitudinal resistance has a minimum, and the Hall resistance has a plateau. As seen, our model describes both SdHO and QHE. The calculated results show that the values of τ/τ_r are different for both processes (see Figure 3). The value of τ/τ_r for SdHO decreases with the magnetic field and approaches unity at $B = 3$ T. At the beginning of the QHE (at $B \approx 3$ T), a phase transition is observed, in which the value of τ/τ_r increases several times compared to the value of τ/τ_r at the end of the SdHO process. In the case of QHE, the value of τ/τ_r decreases slower with increasing magnetic field than in the case of SdHO. As follows from Figure 3, the

SdHO and QHE are the results of the transitional processes because the values of τ_r and τ are comparable. The observed wide plateau in R_{xy} at strong fields can be explained by a decrease in the average collision time of charge carriers.

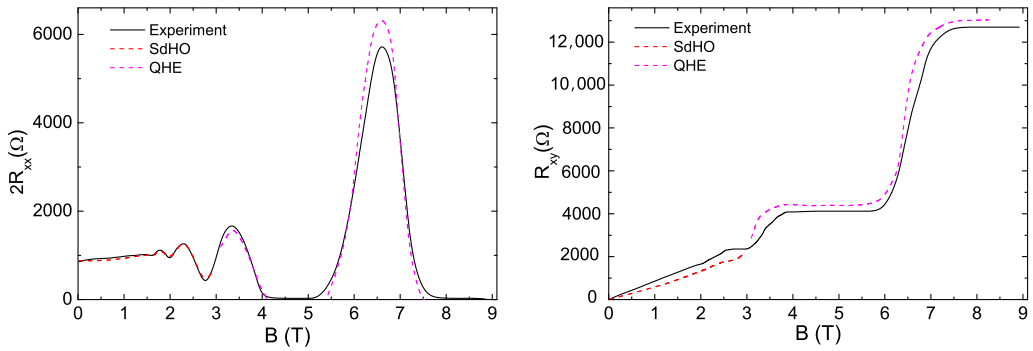

Figure 2. Dependencies of R_{xx} (**left side**) and R_{xy} (**right side**) on the magnetic field B. Experimental results (solid lines) are taken from ref. [17]. Here, the charge carrier mobility is μ = 13,000 cm^{2}V^{-1}s^{-1}, gate voltage $V_g = 15$ V, and temperature of graphene $T_0 = 30$ mK.

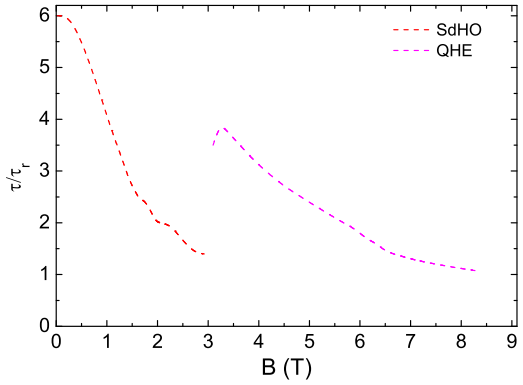

Figure 3. The dependence of τ/τ_r, extracted from the experimental data of ref. [17], on the magnetic field B.

In the QHE, in the region between two plateaus in R_{xy}, the longitudinal resistance R_{xx} has a maximum, while in the center of the plateau, it is a minimum. This phenomenon is explained by antiphase oscillations of R_{xx} and R_{xy}, which are clearly visible in the approximate formulas

$$\begin{aligned} R_{xx}(B) &= \frac{R_{xx0}\left(1+\mu B\exp\left[-\frac{\Gamma^2}{\Gamma^2+B^2}\frac{\tau}{\tau_r}\right]\sin\left[\frac{\left(\Gamma^2+\Gamma/\mu+B^2\right)\mu B}{\Gamma^2+B^2}\frac{\tau}{\tau_r}\right]\right)}{1+\exp\left[-\frac{2\Gamma^2}{\Gamma^2+B^2}\frac{\tau}{\tau_r}\right]-2\exp\left[-\frac{\Gamma^2}{\Gamma^2+B^2}\frac{\tau}{\tau_r}\right]\cos\left[\frac{\left(\Gamma^2+\Gamma/\mu+B^2\right)\mu B}{\Gamma^2+B^2}\frac{\tau}{\tau_r}\right]}, \\ R_{xy}(B) &= \frac{R_{xx0}\mu B\left(1-\exp\left[-\frac{\Gamma^2}{\Gamma^2+B^2}\frac{\tau}{\tau_r}\right]\cos\left[\frac{\left(\Gamma^2+\Gamma/\mu+B^2\right)\mu B}{\Gamma^2+B^2}\frac{\tau}{\tau_r}\right]\right)}{1+\exp\left[-\frac{2\Gamma^2}{\Gamma^2+B^2}\frac{\tau}{\tau_r}\right]-2\exp\left[-\frac{\Gamma^2}{\Gamma^2+B^2}\frac{\tau}{\tau_r}\right]\cos\left[\frac{\left(\Gamma^2+\Gamma/\mu+B^2\right)\mu B}{\Gamma^2+B^2}\frac{\tau}{\tau_r}\right]} \end{aligned} \quad (38)$$

for the axial symmetric system in strong magnetic fields ($\omega_c\tau_r \gg 1$). Here, $R_{xx0} = 1/\sigma_{xx0} = 1/(ne\mu)$.

For the SdHO (Figure 4, left) and QHE (Figure 4, right) [17], the dependencies of the average absolute value of the charge carrier velocity $v(B) = \sqrt{v_x^2(B)+v_y^2(B)}$ on the magnetic field are calculated. At $B \approx 0$ (the SdHO process), $v/c \approx 0.02$ (c is the speed of light in vacuum) and the mean free path $l = v\tau/2 \approx 4$ μm. Typically, the size of graphene used in experiments is of the order of several μm. So in weak magnetic fields, charge carriers move in a ballistic mode. For the QHE at strong magnetic fields ($B > 3$ T) $v_x \ll v_y$

and the off-diagonal resistance or off-diagonal conductance and v_y (π_y) are quantized and have the step-wise behavior. Accordingly, the current component along the y-axis is also a step function of the magnetic field. Note, that the observation of quantized conductance at integer multiples of $2e/h$ at zero magnetic fields in high mobility suspended graphene and GaAs-AlGaAs heterostucture ballistic nanoconstrictions was explained by the assumption of quantized transverse momentum [47–49]. A surprising conclusion of ref. [50] is that the quantized resistance of narrow quasi-one-dimensional (quasi-1D) ballistic channels (point contacts) in the 2D electron gas at $B = 0$ is a limiting case of the QHE in the 2D systems.

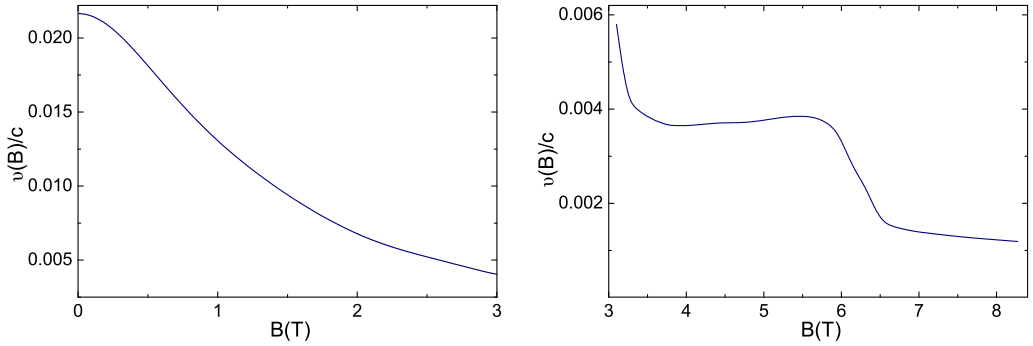

Figure 4. The dependence of v/c on the magnetic field B.

The SdHO has been observed in a graphene sample where the mobility of charge carriers is equal to μ =15,000 cm^{2}V^{-1}s^{-1} [17] (Figure 5). Experimental data show that the value of μ is independent of the temperature up to $T_0 \approx 100$ K [21,24]. As seen in Figure 5, the SdHO are getting smoother as temperature increases, especially at low magnetic fields. The calculated results reproduce this behavior. This is clearly seen for the oscillation term ΔR_{xy} (see Figure 6). The main reason for this is a slight change of the τ/τ_r with increasing T_0. Note, that the values of τ and τ_r are comparable and $\tau \approx \tau_r$ at high magnetic fields. The predicted Hall resistance (Figure 5) shows some plateau-like structure which also becomes smoother with increasing T_0.

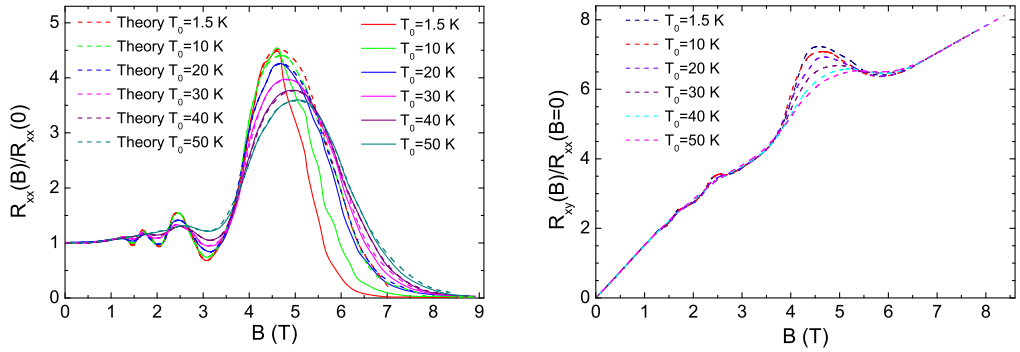

Figure 5. For the SdHO, the longitudinal resistivity resistance (the **left plot**) and the predicted Hall resistance (the **right plot**) in graphene at different temperatures and magnetic fields. Experimental data (solid lines) are taken from ref. [17]. Here the charge carrier mobility in graphene is μ =15,000 cm^{2}V^{-1}s^{-1}.

The SdHO was also measured in a graphene sample with much lower mobility ($\mu = 2700$ cm^{2}V^{-1}s^{-1}) than in the previous case (Figure 7) [19]. The value of τ/τ_r decreases rapidly at weak magnetic fields and approaches $\tau/\tau_r \approx 1$ as the magnetic field increases (see Figure 8). Using these τ/τ_r, we describe well R_{xx}. As seen, the oscillations in R_{xx} are small. The oscillation part ΔR_{xy} of the predicted off-diagonal resistance shows that the plateau-like areas appear at B corresponding to the minima of R_{xx} (Figure 7). Since the scale of the structure of ΔR_{xy} is much smaller than that in Figure 6, the predicted

behavior of ΔR_{xy} or R_{xy} will be difficult to observe in the experiment. However, we should again note some similarities between the SdHO and QHE and the transitional nature of both processes.

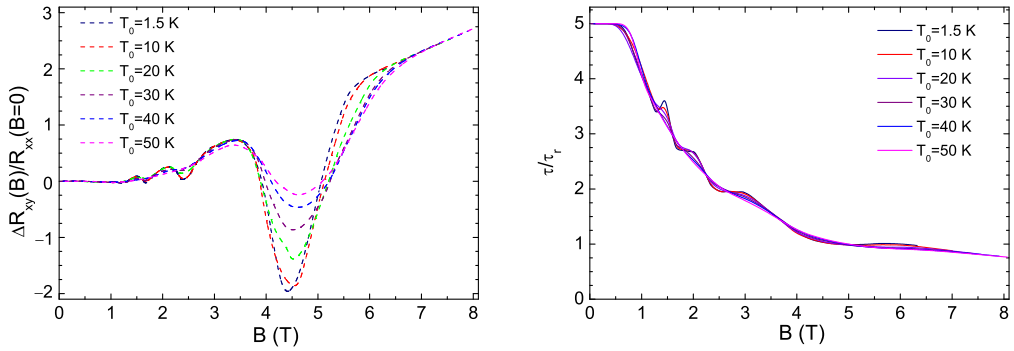

Figure 6. The calculated oscillation part of the Hall resistance (ΔR_{xy}) and τ/τ_r at different temperatures and magnetic fields.

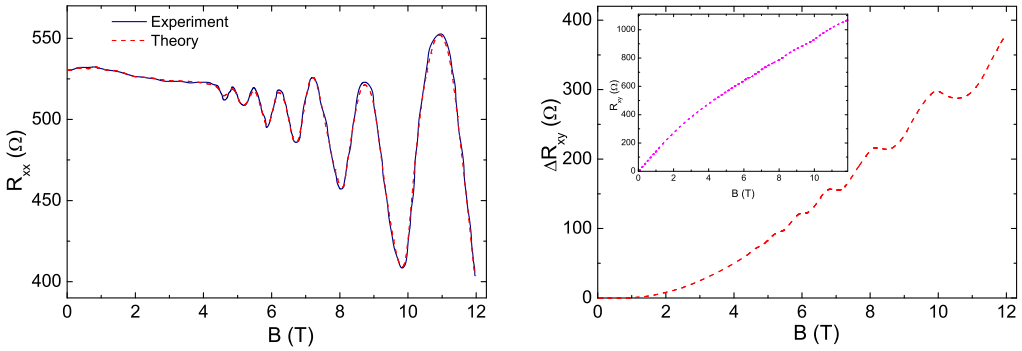

Figure 7. The SdHO (**left**) and the oscillation part ΔR_{xy} of the Hall resistance (**right**). Experimental results (solid line) are taken from ref. [19]. Here, the charge carrier mobility of graphene is $\mu = 2700$ cm^{2}V^{-1}s^{-1}, carrier density $n = 4.38 \times 10^{12}$ cm^2, and temperature $T_0 = 10$ K. The predicted Hall resistance is shown inside.

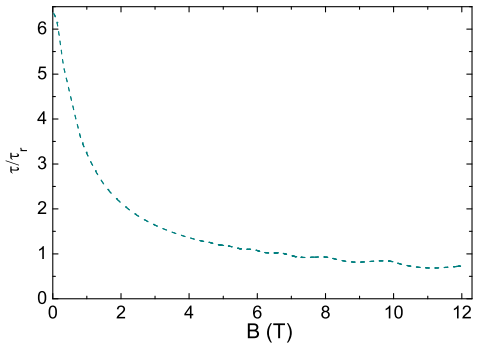

Figure 8. The dependencies of τ/τ_r, extracted from the experimental data of ref. [19], on the magnetic field B.

In Figure 9, the dependencies of the experimental [19] and theoretical diagonal resistance R_{xx} and Hall conductivity σ_{xy} on the carrier density (concentration) n in the graphene are shown at the temperature $T_0 = 4$ K and magnetic field $B = 14$ T. Based on the experimental data of ref. [17], the mobility of charge carriers as a function of the charge density is parameterized as follows $\mu = 0.097 - 0.02|n| + 1.403/(1 + |n|)$ (in unit m^{2}V^{-1}s^{-1}). Using the values of τ/τ_r from Figure 10 (approximately $\tau/\tau_r \sim \sqrt{|n|}$), we obtain quite good

agreement with the experimental data for the R_{xx} and σ_{xy}. Figure 11 shows that the transverse velocity or the transverse momentum is quantized and has a step-wise dependence on n. Thus, the step-like transverse current density J_y as a function of the carrier density is predicted (Figure 12).

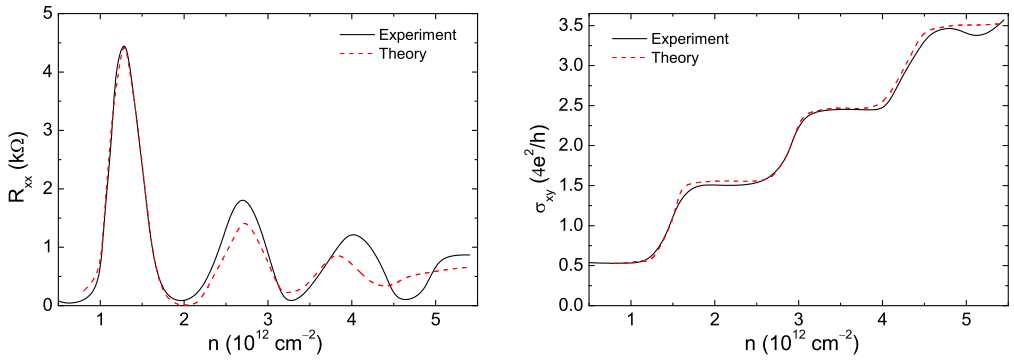

Figure 9. Resistivity R_{xx} and Hall conductivity σ_{xy} as a function of the carrier density n. Experimental results (solid lines) are taken from ref. [19]. Here, the magnetic field is $B = 14$ T and temperature $T_0 = 4$ K.

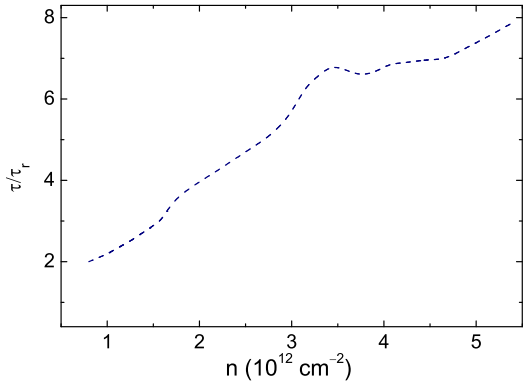

Figure 10. The dependence of τ/τ_r on the carrier density n.

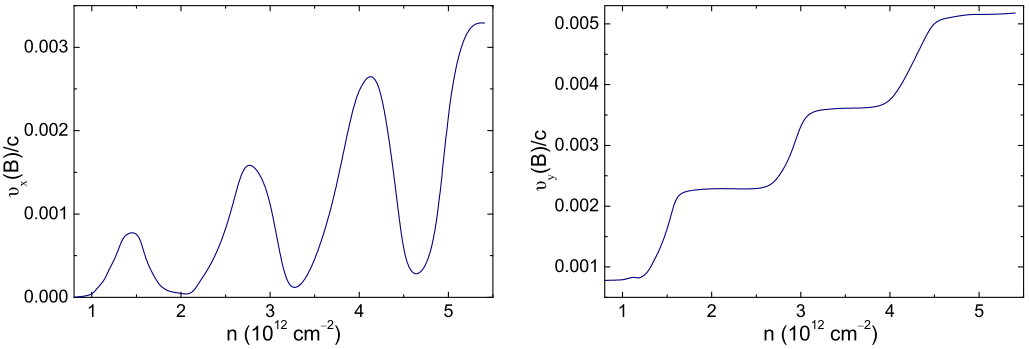

Figure 11. Dependencies of longitudinal v_x and transverse v_y velocities on the carrier density n.

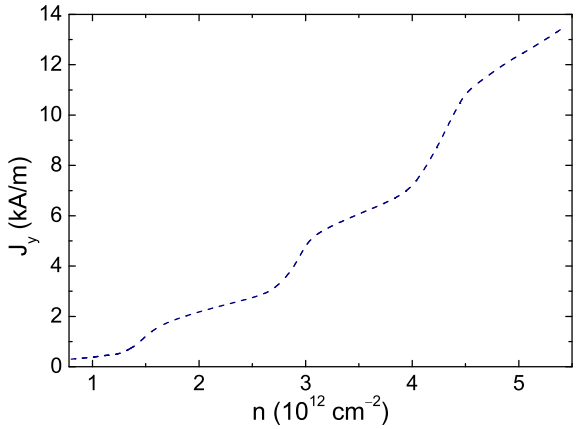

Figure 12. The dependence of the transverse current density J_y on the carrier density n.

We also test the developed model by describing the diagonal resistance R_{xx} and the Hall resistance R_{xy} in the 2DEG GaAs/$Al_xGa_{1-x}As$ [12] (see Figure 13). The experiment was carried out at the temperature $T_0 = 66$ mK, where the charge carrier mobility is $\mu = 52{,}000\ \mathrm{cm^2V^{-1}s^{-1}}$ and the carrier density $n = 1.93 \times 10^{11}\ \mathrm{cm^2}$. As seen from the calculated results in Figure 13, the SdHO and QHE are observed at $B \leq 1.5$ T (weak magnetic fields) and $B > 1.5$ T (strong magnetic fields), respectively, as in the case of graphene [17] (see Figure 2). At $B \approx 1.5$ T, the phase transition occurs between these two processes. The same behavior is observed for the resistance in graphene (Figure 2) [17]. For the 2DEG and graphene, the values of τ/τ_r have almost the same functional dependence on the magnetic field but $\tau/\tau_r(\mathrm{2DEG}) < \tau/\tau_r(\mathrm{graphene})$ (see Figure 14). For both solid materials, in the case of SdHO, the value of τ/τ_r is faster decreasing with increasing B than in the case of QHE. Since the values of τ_r and τ are comparable, the SdHO and QHE are the results of the transitional processes.

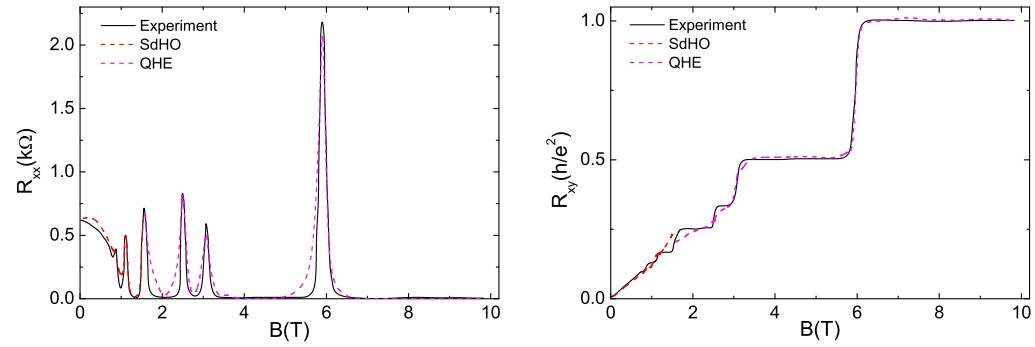

Figure 13. Dependencies of R_{xx} (**left**) and R_{xy} (**right**) on B in 2DEG. Experimental data (solid lines) are taken from ref. [12]. Here the charge carrier mobility is μ = 52,000 $\mathrm{cm^2V^{-1}s^{-1}}$, carrier density $n = 1.93 \times 10^{11}\ \mathrm{cm^{-2}}$, and temperature $T_0 = 66$ mK.

The off-diagonal conductivity (33) is expressed as

$$\sigma_{xy}(B) = -\frac{\sigma_{xx0}\omega_c\tau_r}{1+(\omega_c\tau_r)^2} + \Delta\sigma_{xy}(B),$$

where $\Delta\sigma_{xy}(B)$ is the oscillation part of $\sigma_{xy}(B)$. If the magnetic field is very weak, the oscillation part of the conductance is as follows:

$$\Delta\sigma_{xy}(B) = 2ne\mu B\left(\frac{\tau/\tau_r}{\Gamma} + \mu[1+\tau/\tau_r]\right)\exp(-\tau/\tau_r). \quad (39)$$

The experimental data show that the value of τ/τ_r is much larger at weak magnetic fields, because $\Delta\sigma_{xy}(B) \approx 0$. Since $\tau/\tau_r \approx 1$ at strong magnetic fields, the value of $\Delta\sigma_{xy}(B)$ becomes significantly larger.

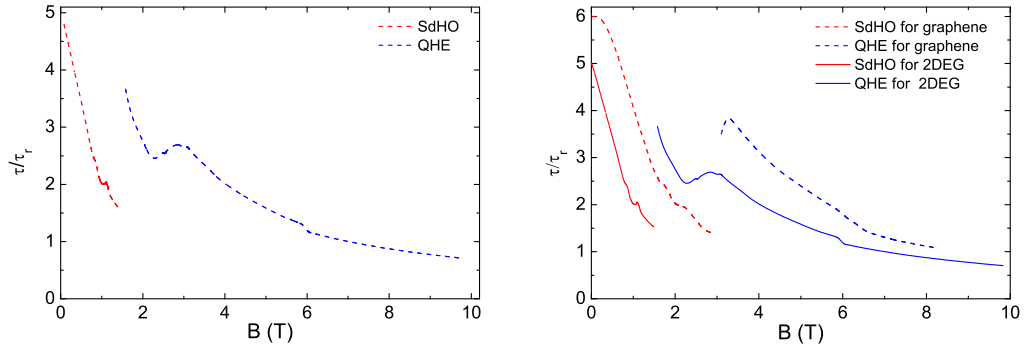

Figure 14. The dependence of τ/τ_r on B (**left**) for 2DEG [12]. The values of τ/τ_r for graphene (dashed lines) [17] and 2DEG (solid lines) [12] are compared (**right**). Here, the charge carrier mobility in graphene is μ = 13,000 cm^{2}V^{-1}s^{-1} and temperature $T_0 = 30$ mK [17]. The charge carrier mobility in 2DEG is μ = 52,000 cm^{2}V^{-1}s^{-1} and temperature $T_0 = 66$ mK.

3.2. Magnetization in Graphene

Using Equation (14) and the time-dependent correlations of the random forces, we derive the $z-$component

$$L_z(\tau) = \langle x(\tau)\pi_y(\tau) - y(\tau)\pi_x(\tau)\rangle = \frac{m\hbar\gamma^2}{\pi}\int_0^\infty d\omega \int_0^\tau dt \int_0^\tau dt' \frac{\coth\left[\frac{\hbar\omega}{2T_0}\right]}{\omega^2+\gamma^2}\cos\left[\omega(t-t')\right]$$
$$\times \left\{\lambda_x\left[B_2(t)C_1(t') - A_1(t)D_2(t')\right] + \lambda_y\left[A_2(t)D_1(t') - B_1(t)C_2(t')\right]\right\} \quad (40)$$

of angular momentum or the magnetization $M(\tau) = neL_z(\tau)/(2m)$. As seen in Figure 15, at weak magnetic fields ($B \leq 3$ T), the magnetization M_z in graphene decreases with increasing B without any oscillations. At strong magnetic fields ($B > 3$ T), plateau-like structures are observed. Even though the plateaus of M_z are slightly different from the ones of R_{xy} (Figure 2), there is a correlation between them: the Hall resistance R_{xy} is constant but the $|M_z|$ decreases in the interval $B \approx 4-6$ T. In the interval $B \approx 6-7.5$ T, the Hall resistance R_{xy} increases sharply, while M_z remains almost constant (see Figures 2 and 15). Note, that the plateaus appear when τ is approaching τ_r with increasing B. The dependence of the predicted magnetization M_z on the magnetic field in graphene with the properties as in Figure 7 is shown in Figure 16. The temperature of a sample is relatively high ($T_0 = 10$ K) and the mobility is relatively small ($\mu = 2700$ cm^{2}V^{-1}s^{-1}); so as a result, the magnetization is small. In Figure 16, plateau-like structures are also formed at $B > 1.5$ T when the values of τ are τ_r are closer to each other.

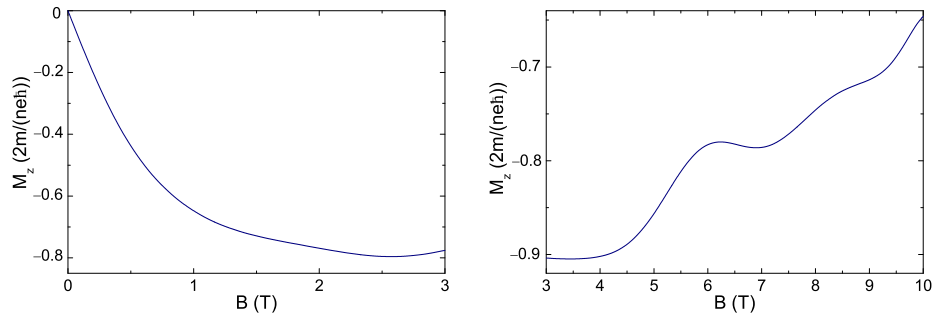

Figure 15. The dependence of magnetization M_z on the magnetic field in graphene at $T_0 = 30$ mK ($m = 0.025\ m_0$ (m_0 is the bare mass of an electron), μ = 13,000 cm^{2}V^{-1}s^{-1} [17]).

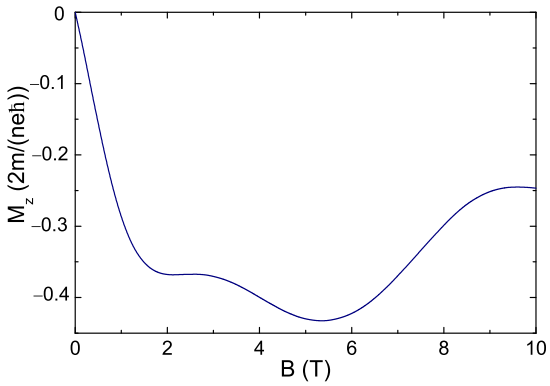

Figure 16. The dependence of magnetization M_z on the magnetic field in graphene at $T_0 = 10$ K ($m = 0.04\ m_0$, μ = 2700 cm^{2}V^{-1}s^{-1} [19]).

3.3. Thermal Conductivity

We assume the same ability of the carriers to carry a charge and transport heat. If the electric energy gradient eE_x in (1) is substituted by the temperature gradient dT_0/dx (the temperature is in energy units), the generating force of particle motion changes from electric to thermal potential, giving rise to thermomagnetic effects. Employing the formula

$$\mathbf{Q} = n\varepsilon_{kin}\dot{\mathbf{q}} \tag{41}$$

for heat flux, the expression for the thermal conductivity tensor is obtained as

$$\kappa(\tau) = \frac{1}{e^2}\varepsilon_{kin}(\tau)\sigma(\tau), \tag{42}$$

where ε_{kin} is the average kinetic energy of the charged particle. In the quasi-equilibrium high-temperature limit ($\tau \to \infty$), one can derive the classical Wiedemann–Franz law [6] for the Lorentz number

$$L = \frac{\kappa}{\sigma T_0} = \frac{1}{e^2} = const. \tag{43}$$

Thus, we obtain a violation of the Wiedemann–Franz law in graphene at low temperatures, which was experimentally observed in ref. [29].

The magnetic field dependencies of the diagonal κ_{xx} and off-diagonal κ_{xy} components of the thermal conductivity in graphene at $T_0 = 30$ mK ($m = 0.025\ m_0$, μ = 13,000 cm^{2}V^{-1}s^{-1} [17]) are shown in Figure 17. At weak magnetic fields, κ_{xx} decreases smoothly with increasing magnetic field. This is more due to the fact that the speed of charge carriers decreases with increasing magnetic field. At $B \approx 0$, the diagonal thermal conductivity is equal to $\kappa_{xx} \approx 1000$ Wm^{-1}K^{-1} and the off-diagonal thermal conductivity is equal to $\kappa_{xy} \approx 0$. When v_y reaches its maximum value, κ_{xy} also reaches its maximum value and then decreases ($\kappa_{xy}^{max} \approx 300$ Wm^{-1}K^{-1}). If the magnetic field is strong enough ($B \geq 3$ T), a noticeably large plateau-like structure is formed in κ_{xx}.

Figure 18 shows the dependence of the diagonal κ_{xx} and non-diagonal κ_{xy} on the magnetic field in graphene ($T_0 = 10$ K, $m = 0.04m_0$, $\mu = 2700$ cm^{2}V^{-1}s^{-1} [19]). The values of τ/τ_r are taken from Figure 8. It is also clear that $\kappa_{xx} > \kappa_{xy}$ at weak magnetic fields. Plateau-like behavior is not observed due to the low mobility of the charge carriers.

Note, that the value of the thermal conductivity in graphene at room temperature and $B = 0$ ranges from $\kappa_{xx} \approx 600$ to 5500 Wm^{-1}K^{-1} [27,28,30]. The calculated κ_{xx} in Figures 17 and 18 are in the intermediate range shown by the experimental data.

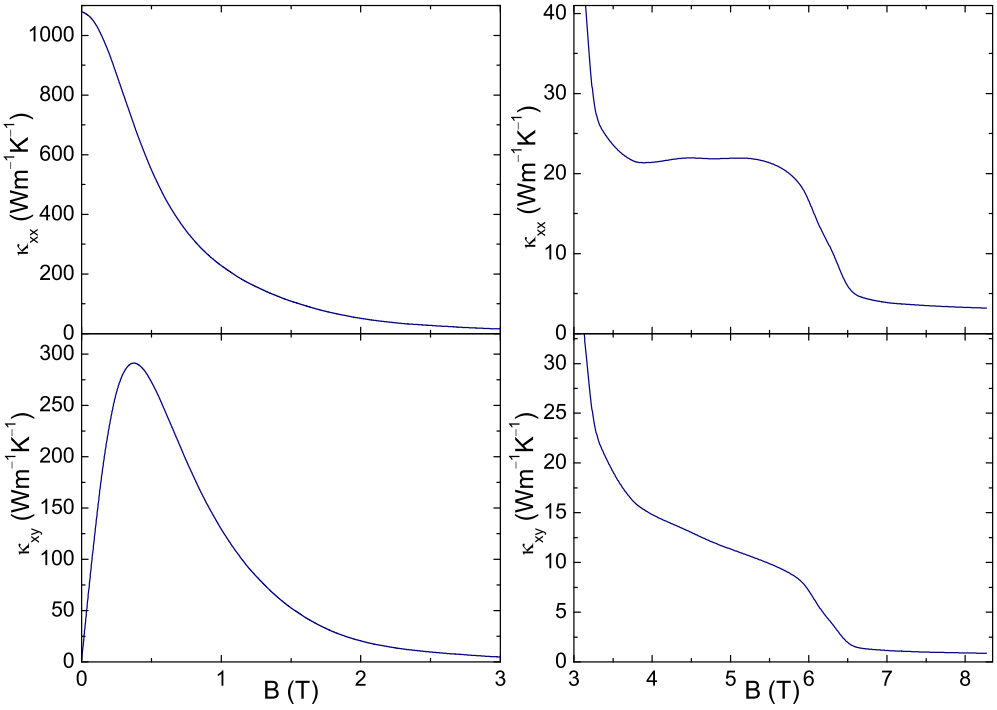

Figure 17. The dependencies of the diagonal κ_{xx} and non-diagonal κ_{xy} components of the thermal conductivity on the magnetic field at $T_0 =$ 30 mK (μ = 13,000 cm^{2}V^{-1}s^{-1} [17]).

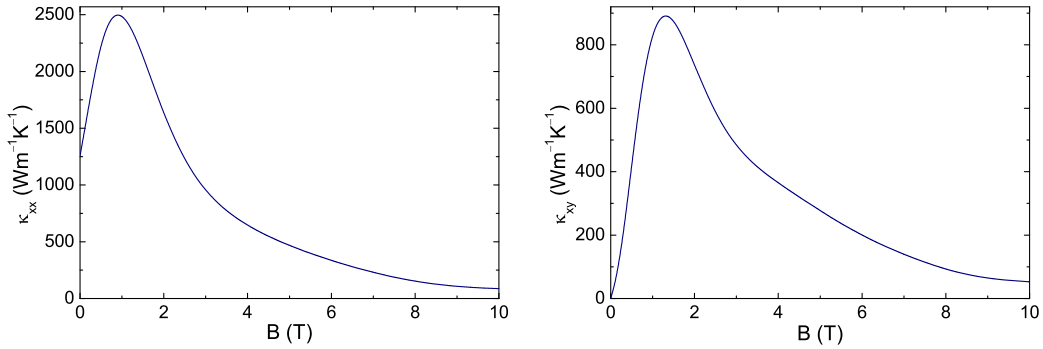

Figure 18. The dependencies of the diagonal κ_{xx} and non-diagonal κ_{xy} thermal conductivities on the magnetic field in graphene at $T_0 = 10$ K ($\mu = 2700$ cm^{2}V^{-1}s^{-1} [19]).

4. Conclusions

Using the non-Markovian quantum Langevin approach and taking into account the coupling between charge carriers and the environment, and two-body effects, we described the SdHO and QHE and predicted thermal conductivity and magnetization in graphene and 2DEG. As shown, the galvano-, and thermo-magnetic effects strongly depend on the relationship between the relaxation and average collision times. The suitable average collision times were adjusted to describe the experimental data. One of the main conclusions of this work is that the values of relaxation and collision times are comparable and, thus, the SdHO and QHE are the results of the transitional processes. As shown for the QHE, the transverse velocity (momentum) is quantized and the transverse current is a step-like function of the magnetic field or charge density. Plateau-like behavior was predicted for the off-diagonal resistance in the SdHO, off-diagonal thermal conductivity, and magnetization in graphene and GaAs/Al_xGa_{1-x}As heterostructure.

Author Contributions: Conceptualization, E.K.A., G.G.A. and N.V.A.; methodology, E.K.A., G.G.A. and N.V.A.; software, E.K.A.; validation, E.K.A., G.G.A. and N.V.A.; formal analysis, E.K.A., G.G.A. and N.V.A.; investigation, E.K.A., G.G.A. and N.V.A.; resources, E.K.A., G.G.A. and N.V.A.; data curation, E.K.A., G.G.A. and N.V.A.; writing—original draft preparation, E.K.A.; writing—review and editing, E.K.A., G.G.A. and N.V.A. All authors have read and agreed to the published version of the manuscript.

Funding: This research received no external funding.

Data Availability Statement: Not applicable.

Conflicts of Interest: The authors declare no conflict of interest.

References

1. Geim A.K. Graphene: Status and Prospects. *Science* **2009**, *324*, 1530. [CrossRef] [PubMed]
2. Novoselov K.S. Nobel Lecture: Graphene: Materials in the Flatland. *Phys. Mod. Rev.* **2011**, *83*, 837. [CrossRef]
3. Castro Neto, A.H.; Guinea, F.; Peres, N.M.R.; Novoselov, K.S.; Geim, A.K. The electronic properties of graphene. *Phys. Mod. Rev.* **2009**, *81*, 109. [CrossRef]
4. Deng, N.; Tian, H.; Zhang, J.; Jian, J.; Wu, F.; Shen, Y.; Ren, T.-L. Black phosphorus junctions and their electrical and optoelectronic applications. *J. Semicond.* **2021**, *42*, 081001. [CrossRef]
5. Xue, X.-X.; Meng, H.; Huang, Z.; Feng, Y.; Qi, X. Black phosphorus-based materials for energy storage and electrocatalytic applications. *J. Phys. Energy* **2021**, *3*, 042002. [CrossRef]
6. Kittel, C. *Introduction to Solid State Physics*, 8th ed.; John Wiley & Sonc, Inc.: Hoboken, NJ, USA, 2005.
7. Komatsubara, K.F. Effect of Electric Field on the Transverse Magnetoresistance in *n*—Indium Antimonide at 1.5 K. *Phys. Rev. Lett.* **1966**, *16*, 1044. [CrossRef]
8. Bauer, G.; Kahlert, H. Hot electron Shubnikov–de Haas effect in n-InSb. *J. Phys. C Solid State Phys.* **1973**, *6*, 1253. [CrossRef]
9. Von Klitzing, K.; Dorda, G.; Pepper, M. New Method for High-Accuracy Determination of the Fine-Structure Constant Based on Quantized Hall Resistance. *Phys. Rev. Lett.* **1980**, *45*, 494. [CrossRef]
10. Tsui, D.C.; Stormer, H.L.; Gossard, A.C. Two-Dimensional Magnetotransport in the Extreme Quantum Limit. *Phys. Rev. B* **1982**, *48*, 1559.
11. Willet, R.; Eisenstein, J.P.; Stormer, H.L.; Tsui, D.C.; Gossard, A.C.; English, J.H. Observation of an even-denominator quantum number in the fractional quantum Hall effect. *Phys. Rev. Lett.* **1987**, *59*, 1776. [CrossRef]
12. Tsui, D.C. Nobel Lecture: Interplay of disorder and interaction in two-dimensional electron gas in intense magnetic fields. *Rev. Mod. Phys.* **1999**, *71*, 891. [CrossRef]
13. Wei, H.P.; Tsui, D.C.; Paalanen, M.A.; Pruisken, A.M.M. Experiments on Delocalization and University in the Integral Quantum Hall Effect. *Phys. Rev. Lett.* **1988**, *61*, 1294. [CrossRef] [PubMed]
14. Li, L.; Yang, F.; Ye, G.J.; Zhang, Z.; Zhu, Z.; Lou, W.; Zhou, X.; Li, L.; Watanabe, K.; Taniguchi, T.; et al. Quantum Hall effect in black phosphorus two-dimensional electron system. *Nat. Nanotechnol.* **2016**, *11*, 593. [CrossRef] [PubMed]
15. Valagiannopoulos, C.A.; Mattheakis, M.; Shirodkar, S.N.; Kaxiras, E. Manipulating polarized light with a planar slab of black phosphorus. *J. Phys. Commun.* **2017**, *1*, 045003. [CrossRef]
16. Hill, S.; Brooks, J.S.; Uji, S.; Takashita, M.; Terakura, C.; Terashima, T.; Aoki, H.; Fisk, Z.; Sarrao, J. Bulk Quantum Hall Effect In η-Mo_4O_{11}. *Synth. Matals* **1999**, *103*, 2667. [CrossRef]
17. Zhang, Y.; Tan, Y.W.; Stormer, H.L.; Kim, P. Experimental observation of the quantum Hall effect and Berry's phase in graphene. *Nature* **2005**, *438*, 201. [CrossRef]
18. Novoselov, K.S.; Giem, A.K.; Morozov, S.V.; Jiang, D.; Zhang,Y.; Dubonos, S.V.; Grigorieva, I.V.; Firsov, A.A. Electric Field Effect in Atomically Thin Carbon Films. *Science* **2004**, *306*, 666. [CrossRef]
19. Novoselov, K.S.; Geim, A.K.; Morozov, S.V.; Jiang, D.; Katsnelson, M.I.; Grigorieva, I.V.; Dubonos, S.V.; Firsov, A.A. Two-dimensional gas of massless Dirac fermions in graphene. *Nature* **2005**, *438*, 197. [CrossRef]
20. Novoselov, K.S.; Jiang, Z.; Zhang, Y.; Morozov, S.V.; Stormer, H.L.; Zeitler, U.; Maan, J.C.; Boebinger, G.S.; Kim, P.; Geim, A.K. Room-temperature quantum Hall effect in graphene. *Science* **2007**, *315*, 1379. [CrossRef]
21. Chen, J.H.; Jang, C.; Xiao, S.; Ishigami, M.; Fuhrer, M.S. Intrinsic and extrinsic performance limits of graphene devices on SiO_2. *Nat. Nanotechnol.* **2008**, *3*, 206. [CrossRef]
22. Du, X.; Skachko, I.; Barker, A.; Andrei, E.Y. Approaching ballistic transport in suspended graphene. *Nat. Nanotechnol.* **2008**, *3*, 491. [CrossRef] [PubMed]
23. Ezawa, Z.F. *Quantum Hall Effects: Field Theoretical Approach and Related Topics*; World Scientific: Hackensack, NJ, USA, 2008.
24. Cooper, D.R.; D'Anjou, B.; Ghattamaneni, N.; Harack, B.; Hilke, M.; Horth, A.; Majlis, N.; Massicote, M.; Vandsburger, L.; Whiteway, E.; et al. Experimental Review of Graphene. *Inter. Sch. Res. Not. Condens. Matter Phys.* **2012**, *2012*, 501686. [CrossRef]
25. Aoki, H.; Dresselhaus, M.S. *Physics of Graphene*; Springer International Publishing: Chem, Switzerland, 2014.
26. Katsnelson, M.I. *The Physics of Graphene*, 2nd ed.; Cambridge University Press: Cambridge, UK, 2020.

27. Balandin, A.A. Thermal properties of graphene and nanostructured carbon materials. *Nat. Mater.* **2011**, *10*, 569. [CrossRef] [PubMed]
28. Pop, E.; Varshney, V.; Roy, A.K. Thermal properties of graphene: Fundamentals and applications. *MRS Bull.* **2012**, *37*, 1273. [CrossRef]
29. Crossno, J.; Shi, J.K.; Wang, K.; Liu, X.; Harzheim, A.; Lucas, A.; Sachdev, S.; Kim, P.; Taniguchi, T.; Watanabe, K.; et al. Observation of the Dirac fluid and the breakdown of the Wiedemann–Franz law in graphene. *Science* **2016**, *351*, 1058. [CrossRef] [PubMed]
30. Sang, M.; Shin, J.; Kim, K.; Yu, K.J. Electronic and Thermal Properties of Graphene and Recent Advances in Graphene Based Electronics Applications. *Nanomaterials* **2019**, *9*, 374. [CrossRef]
31. Ando, T.; Uemura, Y. Theory of Quantum Transport in a Two-Dimensional Electron System under Magnetic Fields. I. Characteristics of Level Broadening and Transport under Strong Fields. *J. Phys. Soc. Jpn.* **1974**, *36*, 4. [CrossRef]
32. Ando, T. Theory of Quantum Transport in a Two-Dimensional Electron System under Magnetic Fields II. Single-Site Approximation under Strong Fields. *J. Phys. Soc. Jpn.* **1974**, *36*, 6. [CrossRef]
33. Ando, T. Theory of Quantum Transport in a Two-Dimensional Electron System under Magnetic Fields. III. Many-Site Approximation. *J. Phys. Soc. Jpn.* **1974**, *37*, 3. [CrossRef]
34. Ando, T. Theory of Quantum Transport in a Two-Dimensional Electron System under Magnetic Fields. IV. Oscillatory Conductivity *J. Phys. Soc. Jpn.* **1974**, *37*, 5. [CrossRef]
35. Zheng, Y.; Ando, T. Hall conductivity of a two-dimensional graphite system. *Phys. Rev. B* **2002**, *65*, 245420. [CrossRef]
36. Van Kampen, N.G. *Stochastic Processes in Physics and Chemistry*; Elsevier: Amsterdam, The Netherlands, 1981.
37. Caldeira, A.O.; Leggett, A.J. Influence of Dissipation on Quantum Tunneling in Macroscopic Systems. *Phys. Rev. Lett.* **1981**, *46*, 211. [CrossRef]
38. Caldeira, A.O.; Leggett, A.J. Quantum tunnelling in a dissipative system. *Ann. Phys.* **1983**, *149*, 374. [CrossRef]
39. Lindenberg, K.; West, B.J. *The Nonequilibrium Statistical Mechanics of Open and Closed*; VCH Publisher: New York, NY, USA, 1990.
40. Isar, A.; Sandulescu, A.; Scutaru, H.; Stefanescu, E.; Scheid, W. Open quantum systems. *Int. J. Mod. Phys. E* **1994**, *3*, 635. [CrossRef]
41. Weiss, U. *Quantum Dissipative Systems*; World Scientific: Singapore, 1999.
42. Kanokov, Z.; Palchikov, Y.V.; Adamian, G.G.; Antonenko, N.V.; Scheid, W. Non-Markovian dynamics of quantum systems. I. Formalism and transport coefficients. *Phys. Rev. E* **2005**, *71*, 016121. [CrossRef] [PubMed]
43. Kalandarov, S.A.; Abdurakhmanov, I.B.; Kanokov, Z.; Adamian, G.G.; Antonenko, N.V. Angular momentum of open quantum systems in external magnetic field. *Phys. Rev. A* **2019**, *99*, 062109. [CrossRef]
44. Lacroix, D.; Sargsyan, V.V.; Adamian, G.G.; Antonenko, N.V. Description of non-Markovian effect in open quantum system with the discretized environment method. *Eur. Phys. J. B* **2015**, *88*, 89. [CrossRef]
45. Alpomishev, E.K.; Adamian, G.G.; Antonenko, N.V. Orbital diamagnetism of two-dimensional quantum systems in a dissipative environment: Non-Markovian effect and application to graphene. *Phys. Rev. E* **2021**, *104*, 054120. [CrossRef]
46. Abdurakhmanov, I.B.; Kanokov, Z.; Adamian, G.G.; Antonenko, N.V. Galvano- and thermo-magnetic effects at low and high temperatures within non-Markovian quantum Langevin approach. *Phys. A* **2018**, *508*, 613. [CrossRef]
47. Van Wees, B.J.; van Houten, H.; Beenakker, C.W.J.; Williamson, J.G.; Kouwenhoven, L.P.; van der Marel, D.; Foxon, C.T. Quantized conductance of point contacts in a two-dimensional electron gas. *Phys. Rev. Lett.* **1988**, *60*, 848. [CrossRef]
48. Wharam, D.A.; Thornton, T.J.; Newbury, R.; Pepper, M.; Ahmed, H.; Frost, J.E.F.; Hasco, D.G.; Peacock, D.C.; Ritchie, D.A.; Jones, G.A. One-dimensional transport and the quantisation of the ballistic resistance. *J. Phys. C Sol. St. Phys.* **1988**, *21*, L209. [CrossRef]
49. Tombros, N.; Veligura, A.; Junesch, J.; Gumarães, H.D.; Vera-Marun, I.J.; Jonkman, H.T.; van Wees, B.J. Quantized conductance of a suspended graphene nanoconstriction. *Nat. Phys.* **2011**, *7*, 697. [CrossRef]
50. Kirczenow, G. Hall effect and ballistic conduction of in a two-dimensional quantum wires. *Phys. Rev. B* **1988**, *38*, 10958. [CrossRef] [PubMed]